Wei *et al. Energy Mater* 2024;4:400062
DOI: 10.20517/energymater.2024.20

Energy Materials

Article

Open Access

Check for updates

Enhancement of Li intercalation kinetics of $LiFePO_4$ nanoparticles with mesoporous carbon

Shaoxin Wei[1], Chaojie Cui[1,2,*], Ying Jin[1], Jin Wang[1], Jian Wang[1], Dongliang Li[2], Weizhong Qian[1,2,*]

[1]Department of Chemical Engineering, Tsinghua University, Beijing 100084, China.
[2]Ordos Laboratory, Ordos 017000, Inner Mongolia, China.

***Correspondence to:** Dr. Chaojie Cui, Department of Chemical Engineering, Tsinghua University, 30 Shuangqing Road, Haidian District, Beijing 100084, China. E-mail: cuicj06@tsinghua.edu.cn; Prof. Weizhong Qian, Department of Chemical Engineering, Tsinghua University, 30 Shuangqing Road, Haidian District, Beijing 100084, China. E-mail: qianwz@tsinghua.edu.cn

How to cite this article: Wei S, Cui C, Jin Y, Wang J, Wang J, Li D, Qian W. Enhancement of Li intercalation kinetics of $LiFePO_4$ nanoparticles with mesoporous carbon. *Energy Mater* 2024;4:400062. https://dx.doi.org/10.20517/energymater.2024.20

Received: 14 Mar 2024 **First Decision:** 19 Apr 2024 **Revised:** 8 May 2024 **Accepted:** 29 May 2024 **Published:** 19 Jun 2024

Academic Editors: Jung Ho Kim, Porun Liu **Copy Editor:** Fangyuan Liu **Production Editor:** Fangyuan Liu

Abstract

Carbon-assisted energy storage in Li-ion batteries is a crucial topic in the era of carbon neutrality. This work reports a remarkable synergistic effect between lithium iron phosphate ($LiFePO_4$, LFP) nanoparticles and mesoporous carbon (MC) that greatly improves the rate performance and cycle performance. The rapid capacitive effect of MC helps establish a local Li^+-rich environment for LFP, enhancing the Li intercalation kinetics inside LFP nanoparticles during discharge. This synergistic effect is quantificationally evaluated using a single-particle model to compare the Li intercalation extent of LFP particles under the presence and absence of MC, which is further confirmed by high-resolution transmission electron microscopy observation, *in-situ* X-ray diffraction characterization and electrochemical impedance spectroscopy test. In addition, the LFP/MC composite cathode exhibits a nearly 100% capacity retention after 1,000 cycles under 1C charge and 10C discharge. Overall, the addition of MC proves to be a very simple but robust method to increase the capacity, power density and cycle life of LFP-based devices.

Keywords: Mesoporous carbon, Li intercalation kinetics, Li-ion battery-capacitors, synergistic effect, *in-situ* X-ray diffraction

INTRODUCTION

The rapid development of renewable electricity from wind power or solar energy presents new challenges

© The Author(s) 2024. **Open Access** This article is licensed under a Creative Commons Attribution 4.0 International License (https://creativecommons.org/licenses/by/4.0/), which permits unrestricted use, sharing, adaptation, distribution and reproduction in any medium or format, for any purpose, even commercially, as long as you give appropriate credit to the original author(s) and the source, provide a link to the Creative Commons license, and indicate if changes were made.

related to the weather-dependent capacity instability, highlighting the need for innovative energy storage solutions that can effectively balance the energy density and power density[1-3]. Typically, Li-ion redox materials offer substantial energy density in battery systems but suffer from poor rate performance due to the slow Li-ion extraction/intercalation reaction[4,5]. To address this issue, the incorporation of certain carbon materials, such as carbon nanotubes (CNTs) and conductive black, or the development of Li-ion cathode material/porous carbon composites has been widely employed to enhance electron transfer within the cathode[6-10]. However, these approaches have not directly improved Li-ion diffusion within the matrix of the cathode materials. While using a significant electrolyte/electrode ratio could promote the diffusion of Li-ion from the bulk phase of electrolyte to the interface of cathode material during high-rate discharge, it comes at the expense of compromising the energy density and substantially increasing the cost of the devices[11-13].

This work reported a remarkable synergistic effect that enhanced both the supply and the diffusion rate of Li-ion in the matrix of nano-sized $LiFePO_4$ (LFP) particles by incorporating mesoporous carbon (MC) materials in large amounts. The optimized mass ratio of LFP to MC was determined to be 3:1, a significantly different amount from the conventional demand as a conductive additive[14]. When charging, the rapid adsorption of PF_6^- anions occurred on the extensive pore surface of MC via the electric double layer capacitor (EDLC) effect[15-17], establishing a local Li^+-rich environment for LFP nanoparticles during discharge. Such a strategy led to a substantial increase in the capacity of LFP when compared with the use of pure LFP. The quantitative evaluation of Li intercalation extent was conducted assuming LFP nanoparticles with an average diameter of 100 nm. The intragranular diffusion velocity of Li-ion was then calculated to demonstrate the accelerated Li intercalation kinetics of LFP nanoparticles in the presence of MC, which was further supported by high-resolution transmission electron microscopy (HRTEM) observation, *in-situ* X-ray diffraction (XRD) characterization and electrochemical impedance spectroscopy (EIS) tests. In addition, LFP particles could maintain a more intact morphology after long cycles with the help of MC and exhibited ultrahigh capacity retention. Our findings not only contributed to a deeper understanding of the synergistic effect between battery materials and capacitive materials but also provided a promising strategy for fabricating the high-performance, hybrid Li-ion battery-capacitors (LIBCs) with excellent energy density, power density and long cycle life[18-23].

EXPERIMENTAL

Preparation of MC

MC material was prepared via a fluidized bed reactor with a diameter of 100 mm using CO_2 activation methods. Commercial activated carbon (YP50-F, Kuraray Co., Ltd., Japan) was used as the raw material. The volume flow rate of CO_2 was 7 L min^{-1} under 1 atm and the reaction temperature was set to 930 °C. After reacting for 9 h, the pore structure of pristine activated carbon was etched adequately by CO_2 to prepare MC material with abundant mesopores.

Electrode preparation and cell assembly

Nano-sized LFP with carbon-coating was purchased from Pulead Technology Industry Co., Ltd., China, without further purification treatment. LFP and MC were firstly mixed by grinding sufficiently to prepare the composite cathodes (abbreviated as LMC, and LMC@3_1 meant the mass ratio of LFP to MC was 3:1). Then, the active material (LFP or LMC), conductive black (Super P), multi-walled CNTs, and polyvinylidene fluoride (PVDF) were mixed in *N*-methyl-2-pyrrolidone (NMP) with a mass ratio of 85:10:1:4. After adequately stirring in a homogenizer, the slurry was coated onto three-dimensional Al foam current collector instead of conventional two-dimensional Al foil, which had been proved to be much more conducive to improve the electrochemical performance of batteries and supercapacitors in previous

work[24,25]. The electrodes were dried at 70 °C for 2 h to remove the NMP solvent and then rolled to 150 μm. For assembling the coin cell, all electrodes were punched into 13 mm disks and further dried at 60 °C overnight in a vacuum oven. The average mass loading of active materials for pure LFP and LMC@3_1 electrodes was 6.94 and 5.56 mg cm^{-2}, where the difference mainly resulted from the distinct tap density between LFP and MC materials. Then, the compaction density of the two electrodes could be calculated by their mass loading and thickness, which were 0.46 and 0.37 g cm^{-3}.

Coin cells (CR2032) were then assembled in the glove box to investigate the electrochemical performance of pure LFP and LMC@3_1 cathodes, where both battery materials (LFP) and capacitive materials (MC) were considered as active materials. Metallic lithium disks (diameter = 16 mm, thickness = 0.6 mm) were used as the anode to assemble the coin cell, and the two electrodes were separated by a polypropylene membrane (Celgard 2400). The space inside the cell was filled with 200 μL organic electrolyte containing 1 mol L^{-1} $LiPF_6$, which was purchased from Zhangjiagang Guotai Huarong New Chemical Materials Co., Ltd, China (LB-4927BY).

Electrochemical tests

Galvanostatic discharging tests were performed by a battery testing system (LAND CT2001A, China) at 25 °C. A voltage range of 2.4-4.2 V was set for all electrochemical measurements with the cells being charged at 1C (1C = 0.17 A g^{-1}) and discharged at different rates from 1C to 50C. Galvanostatic charging tests where the cells were charged at different rates from 1C to 50C and discharged at 1C were also performed to obtain the complete Tafel plot. Cyclic tests were carried out by 1C charge and 10C discharge for 1,000 cycles. It should be noted that both current density and specific capacity were based on the total mass of active materials (including LFP and MC) in the cathodes. Energy (E, Wh kg^{-1}) and power densities (P, W kg^{-1}) were calculated using:

$$E = \frac{I \cdot \int U \, dt}{3600 \times m} \tag{1}$$

$$P = \frac{3600 \times E}{t} \tag{2}$$

Here, I was the discharge current (A), U was the cell voltage (V), t was the discharge time (s), and m (kg) was the total active materials mass in the cathode.

Cyclic voltammetry (CV) and EIS tests were performed by an electrochemical workstation (CHI660E). The scan rates of CV measurement were 1.0 mV s^{-1} between 2.4 to 4.2 V. EIS measurement was conducted at different states of charge (SOC) with a frequency range from 100 kHz to 10 mHz and an applied amplitude of 5 mV. An equivalent circuit model was applied to analyze the EIS results and the parameters were calculated by ZView3.2 software.

Characterization

Crystal structure of LFP was studied by XRD pattern from 10° to 60° 2θ with a scanning rate of 2° min^{-1} using Cu Kα radiation (λ = 0.15406 nm). The numbers of standard XRD patterns used for comparison were PDF#01-078-7911 for LFP and PDF#01-082-9760 for $FePO_4$. Morphology of active materials and electrodes was characterized using a scanning electron microscope (SEM, JEOL JSM-7401) and HRTEM (JEOL JEM-2010), and the lattice fringe spacings of LFP particles in HRTEM images were measured by calculating the average spacing among ten lattice fringes. Element analysis of composite cathode was completed by energy dispersive spectrometer (EDS, Oxford Instruments) mapping. Argon sorption isotherms were measured using Autosorb-iQ2-C at 87 K to analyze the pore structure of LFP and MC. In addition, quenched solid

density functional theory (QSDFT) method was applied to the study of pore size distribution for MC, in which a slit pore shape was assumed. Particle size distribution of MC powders was measured by a Mastersizer 3000 (Malvern, Britain). Electrical conductivity of active material powders was measured by a ST2722 powder resistivity tester (Suzhou Jingge Electronic Co., Ltd., China) under the pressure of 4 MPa, while the electrical conductivity of electrode was measured by a 4-Point Probes Resistivity Measurement System (RTS-9, FOUR PROBES TECH Co., Ltd., China). Electrolyte uptake tests were conducted by immersing the electrode into electrolyte solution, followed by a complete rest until no obvious liquid existed on the electrode surface. The electrolyte uptake was then calculated based on the mass of active materials in the electrode and the mass difference of the electrode before and after immersion.

For the *in-situ* XRD experiments, an *in-situ* electrochemical cell with a high-pure beryllium window was assembled and then charged and discharged at 0.5C and 2C while simultaneously collecting XRD patterns. The 2θ range was set for 24°-38° with 0.02°/step and 0.4 s/step to shorten the collection time per curve and acquire as much original data as possible. Whole pattern fitting (WPF) and Rietveld refinement (RF) were completed using MDI (Materials Data, Inc.) Jade software. The background of the XRD curve was fitted with polynomials (n = 2-5), and the profile shape function (PSF) for all phases was the Pearson-VII function. All parameters that could be refined in the atomic control windows were selected for both LFP and $FePO_4$ phases. The refinement iteration process continued until the values of the agreement R-factor (7%-9%) and R/E (1.01-1.17) were minimal.

RESULTS AND DISCUSSION

Establishment of local Li^+-rich electrolyte region around MC during discharge

In this work, nano-sized LFP and micron-sized MC were used as the battery materials and capacitive materials to fabricate the composite cathode of LIBCs with an Al foam-based current collector. Supplementary Figure 1 showed that the LFP spherical particles (monocrystalline with *Pnma* space group) exhibited a uniform size distribution with a mean diameter of around 100 nm. Supplementary Figure 2 showed the particle size of MC was 1-10 μm with a specific surface area of 2,415 $m^2 g^{-1}$, and the pore volume and mesoporous ratio were 1.209 $cm^3 g^{-1}$ and 20.4% according to the QSDFT fitting result. Owing to the large size of MC materials, the smaller LFP particles surrounded and contacted MC closely in the LMC electrode [Figure 1A] where LFP and MC both acted as active materials. Such structure prompted the establishment of a local Li^+-rich electrolyte region around MC in LMC composite cathode, which allowed the fast Li-ion migration between LFP and electrolyte during discharge. EDS mapping revealed the very uniform distribution of element Al, proving that Al wires existed everywhere and connected each other to greatly reduce the contact resistance between active materials and current collectors owing to the application of 3D Al foam[24,25]. In addition, a significant difference could be seen in the MC particle that element C was present obviously while elements Fe, P, and O were not, proving that LMC was a composite containing LFP and MC and no element was doped on MC. To determine the best composition of LMC, rate performance of composite cathodes with different MC contents was first compared [Supplementary Figure 3A], indicating that the highest specific capacity at 20C-50C could be achieved when the mass ratio of LFP to MC was 3:1 in the composite cathode (i.e., LMC@3_1), which was used to compare with pure LFP cathode in subsequent study.

As follows, we first analyzed the energy storage mechanism of MC in LIBCs. Shellikeri *et al.* had reported the different mechanisms of ion adsorption in the cathode (only activated carbon as active materials) of Li-ion capacitors (LICs) depending on the open circuit potential (OCP)[26]. This may lead to the initial coulomb efficiency (ICE) higher than 100% owing to the capacity contribution arising from the adsorption of Li-ions in MC in the later stage of the first discharge [Supplementary Figure 3B]. In addition, Guo *et al.*

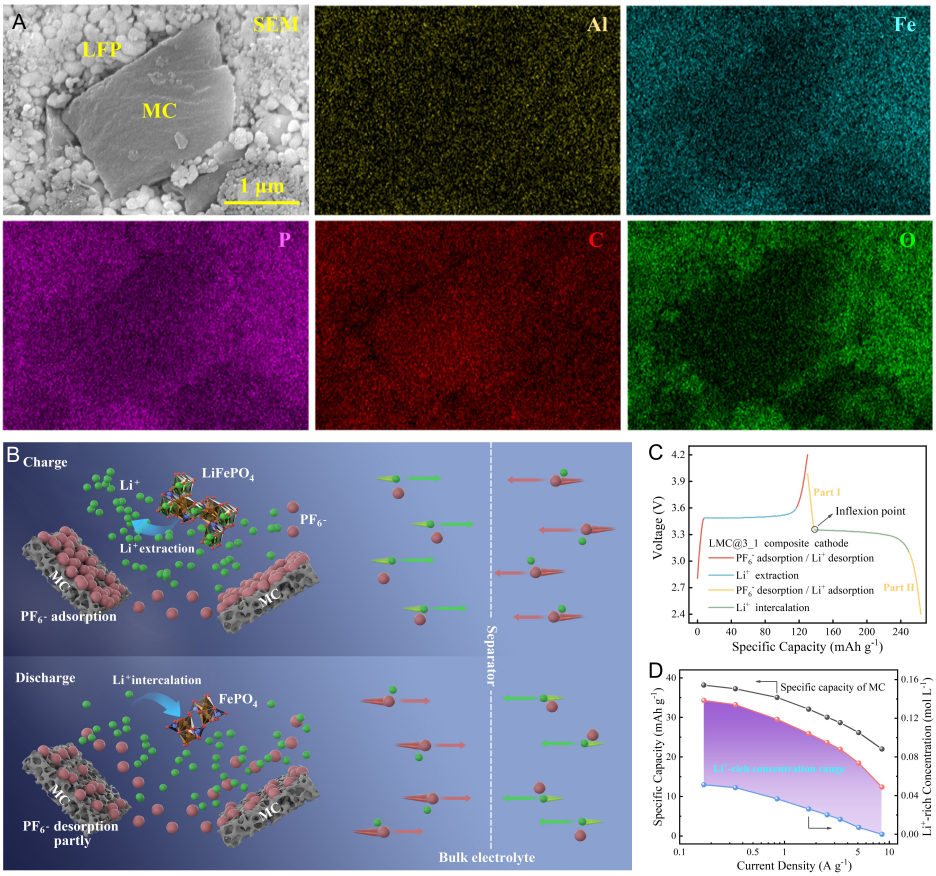

Figure 1. (A) SEM image and EDS mapping results (elements Al, Fe, P, C, O) of LMC@3_1 electrode with LFP and MC as active materials. (B) Schematic illustration of the establishment of local Li^+-rich region around MC, contributing to the fast Li-intercalation kinetics of LFP nanoparticles. (C) Voltage curves of LMC@3_1 cathode under 1C charge/discharge, the corresponding capacitive behavior (PF_6^-/Li^+ adsorption/desorption) and Faraday behavior (Li^+ extraction/intercalation) in different regions were marked. (D) Specific capacity of MC and the Li^+-rich concentration range by MC addition at various current densities.

reported the "recharging phenomenon" in LIBCs, i.e., an inner current flowing from battery materials to capacitive materials could be formed during the rest period after discharge due to their difference in polarization resistance[22]. Stepien *et al.* proved the adsorption of PF_6^- in porous carbon was dominant with respect to Li^+; i.e., the capacitance of adsorbing PF_6^- was larger than that of adsorbing Li^+[15]. Based on these mechanisms, we proposed that MC would also be recharged by LFP upon the rest period after the first discharge, and thus, some adsorptive Li-ions in MC would be desorbed, followed by the adsorption of PF_6^- in MC during subsequent charge. It may be hard to affirm if all adsorptive Li-ions were desorbed during such recharging processes. However, it was definite that the adsorption and desorption of PF_6^- could occur both in the whole range higher than OCP and in some range lower than OCP, contributing to the capacitive effect of MC in LIBCs.

Considering the adsorption and desorption of PF_6^- in MC, Figure 1B illustrated the establishment of a local Li^+-rich region around MC and Figure 1C showed the corresponding voltage curves of LMC@3_1 cathode under 1C charge/discharge. Upon charge, PF_6^- anions were adsorbed rapidly on the pore surface of MC due to the EDLC effect (two red oblique lines in Figure 1C), and Li-ions would also be extracted from LFP

crystals when the voltage reached a specific value (blue horizontal line in Figure 1C), thus generating amounts of free Li-ions in the electrolyte around MC. Meanwhile, Li-ions in the bulk electrolyte phase would migrate from the cathode to the anode side under the electric field effect. On account of the slow Li-ion diffusion rate in electrolytes, a local Li^+-rich electrolyte region formed around the MC particles. When discharging, partial desorption of PF_6^- anions would happen firstly, corresponding to the yellow oblique line I in Figure 1C. As the voltage decreased to a specific value (defined as "inflexion point" meaning the shift from capacitive behavior to Faraday behavior during discharge), Li-ions were intercalated to $FePO_4$ crystals to generate LFP (green horizontal line in Figure 1C). It was worth noting that some PF_6^- anions did not undergo desorption until the Li-intercalation of $FePO_4$ (i.e., the redox reaction inside LFP particles) completed, which corresponded to the yellow oblique line II in Figure 1C[27-29]. Therefore, the local Li^+-rich electrolyte region around MC was still present to enhance the Li-intercalation kinetics of LFP during discharge. Based on two extreme cases (one was adsorption/desorption of PF_6^- occurred in the entire range and another was it only occurred in that higher than OCP), we derived the Li^+-rich concentration range by MC addition according to the specific capacity of pure MC cathode at various current densities (Figure 1D, Supplementary Figure 4, Supplementary Table 1, detailed calculation process in Supplementary Calculation 1). It could be seen that the Li^+-rich concentration showed the same trend as the specific capacity, i.e., decreasing with the increase of current density. The Li^+-rich concentration in LMC@3_1 cathode could reach 0.139 mol L^{-1} at a low current density of 0.17 A g^{-1} owing to the EDLC effect of MC, which was comparable to the original Li-ion concentration in bulk electrolyte (1 mol L^{-1}). Even at a current density as high as 8.50 A g^{-1}, the Li^+-rich concentration could remain 0.049 mol L^{-1}, proving the superiority of adding MC for increasing the concentration gradient of Li-ions. In summary, the addition of sufficient amounts of MC in the LFP electrode did render a local Li^+-rich electrolyte region to improve the Li-ion diffusion performance from electrolyte to LFP and then accelerate the electrochemical reaction.

Quantitative analysis of the synergistic effect between LFP and MC and the Li intercalation kinetics of single LFP particle

Figure 2A showed the CV results of pure LFP and pure MC cathodes at a scan rate of 1.0 mV s^{-1}, which exhibited a couple of typica l redox peaks for LFP and an approximate rectangle shape for MC. In addition, the current density in pure LFP was far larger than that in pure MC on account of the lower capacity of MC compared with LFP. To clearly observe the synergistic effect between battery materials and capacitive materials, a CV curve derived from the linear weighted sum of pure LFP and pure MC cathodes according to their mass ratio (3:1) was compared with that of the LMC@3_1 cathode. It could be seen from Figure 2B that the intensity of redox peaks in LMC@3_1 was much stronger than that of the linear weighted sum of pure LFP and MC, proving the faster and more complete redox reaction occurred inside LFP particles in the presence of MC, i.e., a favorable synergistic effect existed between LFP and MC materials. Besides, the CV curve of LMC@3_1 also showed the approximate rectangle shape in the low (2.4-2.8 V) and the high voltage regions (3.9-4.2 V)[29,30], demonstrating that the capacitive process (adsorption/desorption of PF_6^- anions) happened both before and after the redox process of LFP. This result confirmed the viewpoint in Figure 1B that only a part of PF_6^- anions had desorbed from the pore surface of MC when Li-intercalation reaction proceeded. On the other hand, a smaller potential difference between oxidation and reduction peaks could be observed in the LMC@3_1 cathode as well, indicating the slighter electrode polarization and the better reversibility of LFP particles with the enhancement effect of MC, which was attributed to the higher electrical conductivity [Supplementary Figure 5], the better Li-ion diffusion performance and the faster electrochemical reaction rate that would be further verified in subsequent EIS study.

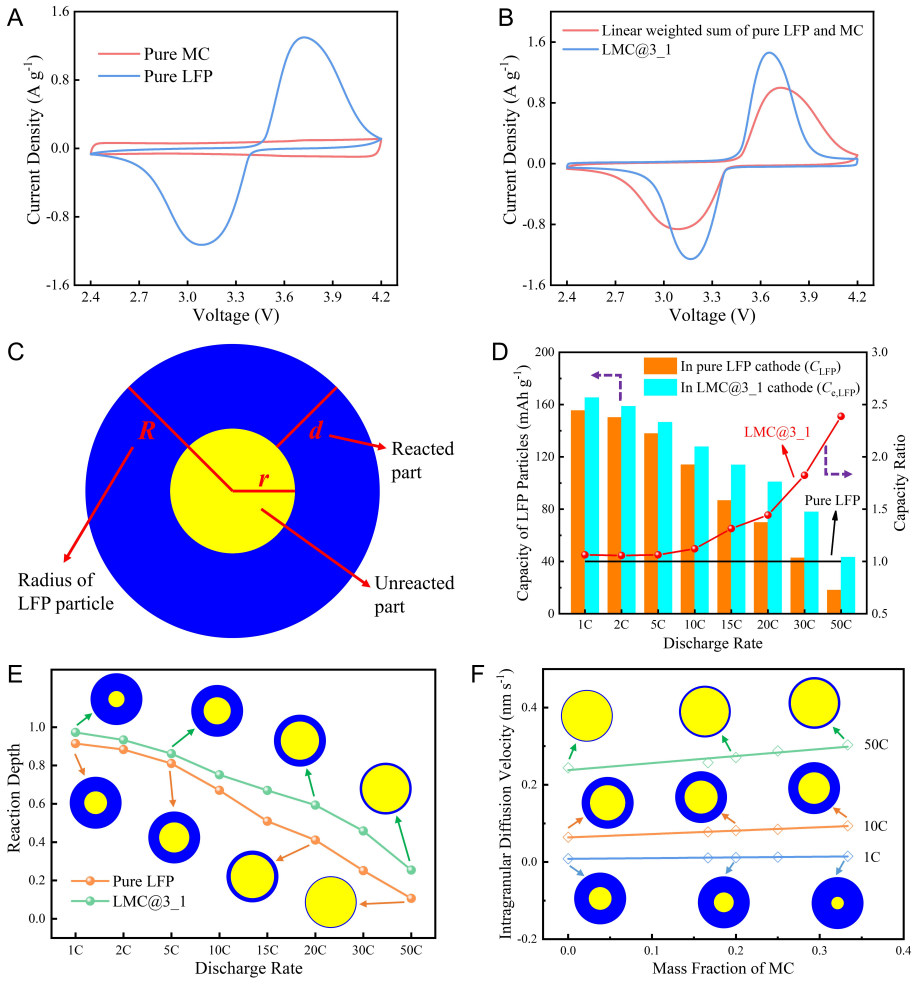

Figure 2. (A) CV results of pure LFP and pure MC cathodes at scan rate of 1.0 mV s^{-1}. (B) CV results of LMC@3_1 cathode at scan rate of 1.0 mV s^{-1} and the comparison with that of linear weighted sum of pure LFP and pure MC cathodes. (C) Simplified model of single LFP spherical particle considering one-dimensional diffusion channel of Li-ion inside LFP, the blue ring and yellow circle meant the reacted part and unreacted part. (D) Capacity of LFP particles in pure LFP (C_{LFP}) and in LMC@3_1 ($C_{e,LFP}$) cathodes, and the capacity ratio of LMC@3_1 comparing with that of pure LFP (CR = 1) under various discharge rates. (E) Reaction depth of LFP particles in pure LFP and in LMC@3_1 cathodes under various discharge rates, along with the illustration of Li intercalation extent in LFP particle. (F) Linear relationship between intragranular diffusion velocity and the mass fraction of MC in LMC composite cathodes, along with the illustration of Li intercalation extent in LFP particles.

Redox performance of pure LFP and capacitive performance of pure MC could be easily measured in advance, so it was possible to quantificationally evaluate the synergistic effect between battery materials (LFP) and capacitive materials (MC). One important thing to note was that the additional capacity owing to the synergistic effect was supposed to originate from the more capacity release of LFP particles, as the capacity of MC mainly depended on its specific surface and conductivity should remain nearly unchanged in the composite cathode. Thus, different from the calculation of additional capacity "ΔC" based on the mass of both battery materials and capacitive materials in previous work[31,32], we proposed a novel method to evaluate the synergistic effect more precisely. Moreover, the present LFP nanoparticles were close to spherical shape and had a narrow size distribution [Supplementary Figure 1], which allowed us to obtain the Li intercalation kinetics of single LFP particles.

As shown in Figure 2C, the LFP particle was simplified to a perfect sphere of radius R (equaled to 50 nm in this work). Taking the "shrinking core" model in previous work as a reference[33-36], we assumed that the Li-intercalation reaction always occurred evenly from the outside to the inside, considering the one-dimensional diffusion channel of Li-ion in the matrix of LFP crystals. Accordingly, some indexes could be defined and calculated by:

$$C_e = C_{e,LFP} \times f_{LFP} + C_{MC} \times f_{MC} \quad (3)$$

$$\text{Capacity Ratio} = \frac{C_{e,LFP}}{C_{LFP}} \quad (4)$$

$$\text{Reaction Depth} = \frac{C_{e,LFP}}{C_{t,LFP}} = \frac{V_{reaction}}{V_{particle}} = 1 - \left(1 - \frac{d}{R}\right)^3 \quad (5)$$

$$\text{Intragranular Diffusion Velocity} = \frac{d}{t} \quad (6)$$

Here, C_e and $C_{t,LFP}$ were the capacity of various cathodes obtained experimentally and the theoretical capacity of LFP (170 mAh g^{-1}), while C_{MC} and C_{LFP} were the specific capacities delivered by pure MC and LFP cathodes. The f_{LFP} and f_{MC} were the mass fraction of LFP and MC; d was the intragranular diffusion length, and t was the discharge time. Specially, $C_{e,LFP}$ obtained from Equation (3) was the actual capacity delivered by LFP in composite cathodes, which was more suitable to evaluate the synergistic effect and analyze the Li intercalation kinetics. The values of calculated $C_{e,LFP}$ and capacity contribution of MC (CC_{MC}) in various LMC composite cathodes were listed in Supplementary Table 2. Further, the capacity ratio (CR) was used to compare the capacity of LFP with or without MC addition according to Equation (4), which was directly associated with the synergistic effect. Reaction depth (RD) with a value range from 0 to 1 represented the Li intercalation extent in LFP particles during discharge, and the intragranular diffusion length d could be then obtained according to Equation (5). More importantly, intragranular diffusion velocity (IDV) could also be calculated according to Equation (6) to compare the Li intercalation kinetics of LFP in the presence of MC or not. The values of CR, RD and IDV of LMC composite cathodes with different mass ratios of MC under various discharge rates were shown in Supplementary Figure 6 in detail. Herein, LMC@3_1 was chosen to compare with pure LFP in subsequent analysis because of its excellent rate performance.

Figure 2D showed that the specific capacity of LFP particles in LMC@3_1 cathode ($C_{e,LFP}$) was always higher than that in pure LFP cathode (C_{LFP}) under discharge rates of 1C-50C, and thus the CR values of LMC@3_1 were always larger than 1 (represented pure LFP), indicating the more capacity release of LFP particles as adding MC. In addition, the CR value also increased drastically when the discharge rate exceeded 10C. Quantitatively, this value was 1.12 at 10C and increased to 1.44 and 2.39 at 20C and 50C, demonstrating that the addition of MC in large amounts helped build a much stronger synergistic effect with LFP upon higher current density. These results convincingly validated the existence of a synergistic effect between battery materials (LFP) and capacitive materials (MC), which could be quantificationally evaluated by the calculation of CR. Further, Li intercalation kinetics of LFP could also be analyzed based on the single-particle model. As shown in Figure 2E, RD decreased with the increase of discharge rates for both cathodes, and the LMC@3_1 cathode always exhibited larger RD values than the pure LFP cathode at all rates. Strikingly, the higher the current density was, the larger the gap existed for the RD values between that with and without adding MC. This proved that the Li intercalation extent of LFP particles reduced enormously under high rates owing to the severe electron polarization and ion polarization. It, however, could be alleviated effectively with the addition of MC. Moreover, the value of IDV was enhanced enormously with

the discharge rate [Figure 2F]. It reached 0.24 nm s^{-1} at 50C for pure LFP (corresponding to the mass fraction of MC with 0), nearly 30 times that at 1C (8.5×10^{-3} nm s^{-1}). That meant that the current density increased by 50 times, but the Li diffusion velocity just increased by 30 times, which well explained the limitation of ion diffusion under high current density. In comparison, the value of IDV at 50C for LMC@3_1 (corresponding to the mass fraction of MC with 0.25) was 0.29 nm s^{-1} with 1.2 times larger than that for pure LFP, demonstrating that the limitation of ion diffusion did alleviate, to some extent, by adding MC. Specifically, IDV also exhibited a linear relationship with the mass fraction of MC, and the positive slope was improved with increasing discharge rate (from 0.019 nm s^{-1} at 1C to 0.18 nm s^{-1} at 50C). This validated that the rapid EDLC response of MC offering a Li^+-rich environment for LFP greatly enhanced the Li intercalation kinetics during discharge, especially at a high rate of 10C-50C. The above results verified a sound synergistic effect between LFP and MC, not merely a linear addition of redox effect and EDLC effect, where MC could also enhance the Li intercalation kinetics of LFP, not merely acted as conductive additives as in most of previous work[14,37,38].

Analysis of Li intercalation extent and phase transition by HRTEM observation and in-situ XRD characterization

The Li intercalation extent of LFP nanoparticles in pure LFP and LMC@3_1 cathodes after high-rate discharging was directly observed by HRTEM imaging. After discharging at 5C, some LFP particles in pure LFP cathode were intercalated with Li-ions completely [Figure 3A], while others were intercalated partially to generate the intermediate Li_xFePO_4 phase [Figure 3B and C]. Previous work had proved the presence of an intermediate Li_xFePO_4 phase during discharge of LFP particles by *ex-situ* and *in-situ* XRD study[39-41]. Here, the lattice fringe spacings of 3.83-3.85 Å in Figure 3B and C, between 3.74 Å (corresponding to (210) plane of $FePO_4$) and 3.91 Å (corresponding to (210) plane of LFP), demonstrated the incomplete Li intercalation process after 5C discharge and thus led to the formation of intermediate Li_xFePO_4 phase. A similar phenomenon, but with more LFP phase present, could be found in HRTEM images of LFP particles in LMC@3_1 cathode after 5C discharge [Figure 3D-F], and the phase distribution in Figure 3E confirmed the reasonability of assumption in Figure 2C that the Li intercalation proceeded preferentially on the outside of LFP particles. Considering the illustration of Li intercalation extent in Figure 2E, where both LFP and $FePO_4$ phases were abundant, the observed intermediate Li_xFePO_4 phase might be the mixed crystal of LFP and $FePO_4$, which lay in the transition region or interface between these two phases[33,42,43].

After discharging at a high rate of 20C, the Li intercalation extent of LFP particles in pure LFP and LMC@3_1 cathodes exhibited a huge difference. The lattice fringe spacings of 4.94 and 4.43 Å observed in pure LFP cathode were slightly larger than that of 4.91 and 4.30 Å (corresponding to standard $FePO_4$ phase), which should be attributed to the intercalation of bits of Li-ions into the lattice of $FePO_4$ [Figure 3G-I]. However, owing to the extremely low Li intercalation extent of LFP particles at such a high discharge rate, the intercalated-free $FePO_4$ phase was dominant, and there were few LFP phases observed. While for the LMC@3_1 cathode, a much more abundant LFP phase could be observed in Figure 3J-L on account of the enhancement effect of MC to the Li intercalation kinetics of LFP particles compared with that in pure LFP cathode. In addition, the ordered arrangement of LFP and $FePO_4$ phases in Figure 3K again verified the direction of Li intercalation from the outside to the inside, leading to the formation of the LFP phase at the particle edges and the extended lattice fringe spacings in $FePO_4$ phase due to the incomplete intercalation process. These direct observations in HRTEM images revealed the intercalation behavior of Li-ions inside LFP nanoparticles, demonstrating that the addition of MC enormously increased the Li intercalation extent and, thus, effectively improved the capacity release of LFP-based cathode during high-rate discharge.

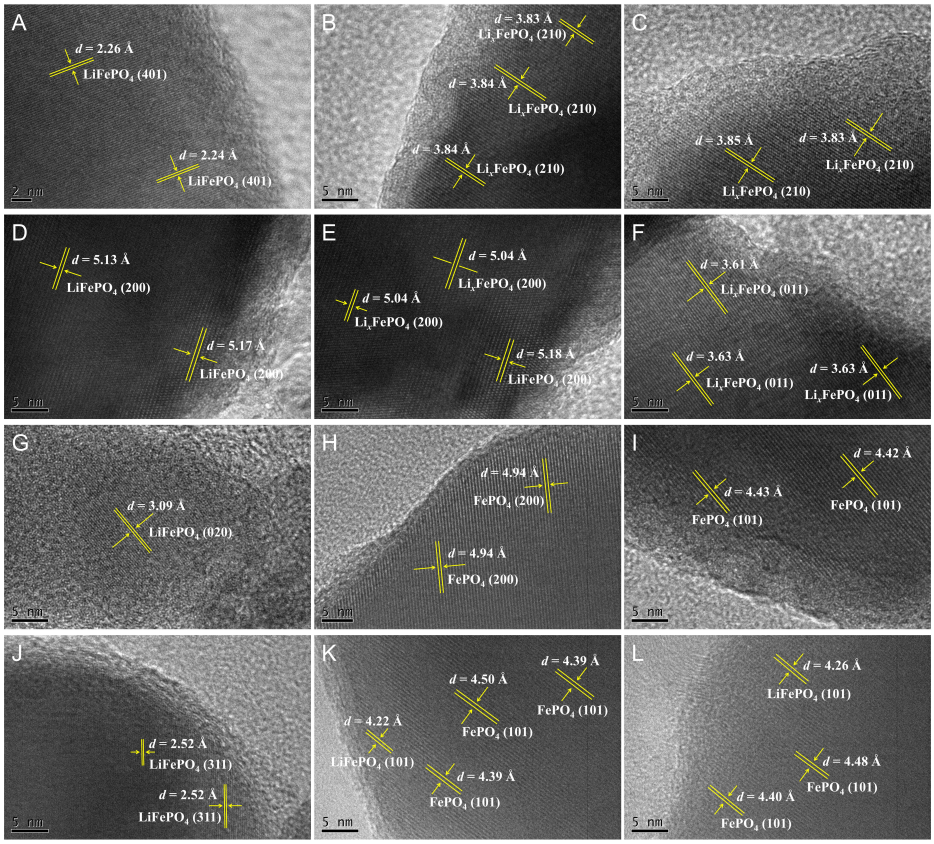

Figure 3. HRTEM images of LFP nanoparticles in pure LFP and LMC@3_1 cathodes after discharging at 5C and 20C, involving the lattice fringe spacings and corresponding phase composition and lattice plane. (A-C) LFP particles in pure LFP cathode after 5C discharge. (D-F) LFP particles in LMC@3_1 cathode after 5C discharge. (G-I) LFP particles in pure LFP cathode after 20C discharge. (J-L) LFP particles in LMC@3_1 cathode after 20C discharge.

To deeply understand the difference of changes in phase composition and crystal structure of LFP with or without MC during the electrochemical reaction, we further conducted the *in-situ* XRD experiments under 0.5C and 2C charge/discharge using the *in-situ* cell of reflection type. Supplementary Figure 7 showed a part of original XRD patterns and the match of peak position to standard cards. Upon charge at 0.5C, the major peaks changed from 25.59°, 29.74°, 32.24°, 35.62°, 36.57° to 25.79°, 30.29°, 30.89°, 36.68°, 37.43° accordingly, which indicated the Li extraction of LFP and the formation of $FePO_4$ phase during charge process [Figure 4A and B]. Additionally, the opposite changes from $FePO_4$ to LFP happened when discharging. WPF and RF were performed for acquiring the quantitative results of phase composition and crystal structure. Figure 4C presented the mass fraction evolution of LFP and $FePO_4$ during 0.5C charge (from 0% to 100% SOC) and 0.5C discharge (from 100% to 0% SOC). In detail, the addition of MC resulted in the timely appearance of the cross-point (50% LFP phase and 50% $FePO_4$ phase) at 55% SOC during charge, which increased to 62% SOC for pure LFP. Besides, complete Li extraction occurred at 86% SOC as adding MC, while it was associated at 100% SOC for pure LFP. These all indicated the slower Li extraction rate of LFP without MC. Moreover, it was also observed that the $FePO_4$ phase kept for a much wider SOC range in LMC@3_1, which could be ascribed to the capacitive behavior of MC and, thus, no phase transition around 100% SOC (i.e., at the end of charge and the beginning of discharge). During the discharge process, the complete phase transition from $FePO_4$ to LFP was achieved from 73% to 7% SOC (a practical range of 66% SOC) for LMC@3_1, while it was from 86% to 0% SOC (a practical range of 86% SOC) for pure LFP. This comparison directly verified the Li intercalation kinetics of LFP particles could be greatly enhanced by large

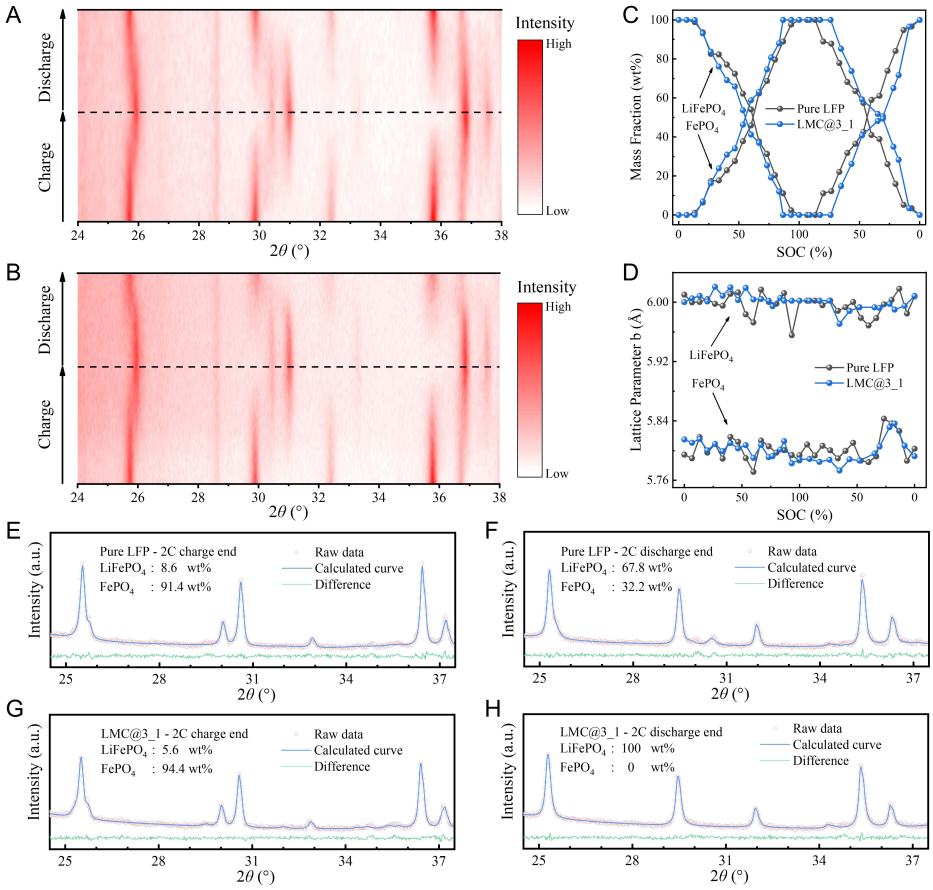

Figure 4. Heat map of original *in-situ* XRD patterns under 0.5C charge/discharge: (A) pure LFP cathode, (B) LMC@3_1 cathode. Whole pattern fitting and Rietveld refinement results of original *in-situ* XRD patterns at different SOC under 0.5C charge/discharge: (C) mass fraction of $LiFePO_4$ and $FePO_4$, (D) lattice parameter b of $LiFePO_4$ and $FePO_4$. Whole pattern fitting and Rietveld refinement results of original *in-situ* XRD patterns at the end of 2C charge and discharge: (E) end of 2C charge for pure LFP, (F) end of 2C discharge for pure LFP, (G) end of 2C charge for LMC@3_1, (H) end of 2C discharge for LMC@3_1.

amounts of MC. In addition, variation of lattice parameter b of LFP and $FePO_4$ reflected the changes of crystal volume in the diffusion orientation of Li-ions. As shown in Figure 4D, the lattice parameter b in the LMC@3_1 cathode changed much more slightly compared with that in pure LFP, which revealed a more uniform reaction inside LFP particles in the presence of MC.

Besides, the *in-situ* XRD patterns were collected under a high charge/discharge rate of 2C, and the original XRD patterns at the end of charge/discharge were further processed by WPF and RF to obtain the quantitative results of phase composition [Figure 4E-H]. For a pure LFP cathode, there was still 8.6 wt% LFP residual at the end of 2C charge, and 32.2 wt% $FePO_4$ remained unable to finish the Li intercalation process when 2C discharge completed. In sharp contrast, there was only 5.6 wt% LFP residual in the LMC@3_1 cathode at the end of 2C charge, and all $FePO_4$ was completely intercalated with Li-ions during 2C discharge. The above results in Figures 2-4 all validated that the rapid capacitive effect of MC enhanced the Li intercalation kinetics of LFP nanoparticles in LMC@3_1 cathode by comparing with pure LFP cathode.

Electrochemical characterization of pure LFP and LMC@3_1 cathodes

As follows, EIS results at various SOC were analyzed using equivalent circuit models to understand the enhancement of Li-ion diffusion performance and electrochemical reaction rate of LFP by adding MC. The

parameters of R_S, $C_{SEI}//R_{SEI}$, $Q_{dl}//R_{ct}$, $Q_{neg}//R_{neg}$ and Q_w in the equivalent circuit model of Figure 5A were explained in Supplementary Figure 8, and the key fitting parameters at various SOC from 10% to 90% were listed in Supplementary Table 3. Specially, charge transfer resistance (R_{ct}) represented the difficulty for the electrochemical reaction to occur, and the linear part in the low-frequency region was related to the Li-ion diffusive behavior inside LFP particles and expressed by a constant phase element Q_w in series. As shown in Figure 5A, a smaller diameter of the arc was observed in the mid-high-frequency region for the LMC@3_1 cathode, indicating the lower R_{ct} for combining Li-ions and electrons in the interface of LFP/electrolyte by adding MC. Quantitatively, the average R_{ct} value from 10% to 90% SOC was 6.03 Ohm for LMC@3_1, much smaller than that (10.64 Ohm) for pure LFP [Figure 5B]. This explained well that the local Li^+-rich region generated by EDLC effect of MC was favorable to the charge transfer process in LFP/electrolyte interface and, thus, accelerated the subsequent electrochemical reaction inside LFP particles. On the other hand, the solid-phase Li-ion diffusion coefficient (D_{Li^+}, $cm^2\ s^{-1}$) at various SOC could also be obtained according to the linear fitting of Z_{Re} to $\omega^{-0.5}$ in the low-frequency region[44] (Figure 5C; 0.01-0.1 Hz in this work as the inset of Figure 5A; detailed calculation process in Supplementary Calculation 2). The average D_{Li^+} value was 5.739×10^{-17} $cm^2\ s^{-1}$ for LMC@3_1, approximately six times larger than that (9.184×10^{-18} $cm^2\ s^{-1}$) for pure LFP. This result further validated that the local Li^+-rich region generated by EDLC effect of MC indeed increased the Li-ion diffusion rate inside LFP particles, a key factor to improve the electrochemical performance of LFP under high current density.

In addition, the voltage-capacity curves at 15C charge/discharge (voltage curves at other rates were shown in Supplementary Figure 9) were plotted and used to calculate the overpotential during charge (η_{ch}) and discharge (η_{dis}), as shown in Figure 5D. Overpotential was defined as the difference between thermodynamic potential (3.43 V *vs.* Li/Li^+ for LFP) and experiment data at half charge/discharge in this work[45,46]. LMC@3_1 exhibited lower charge voltage, higher discharge voltage and higher specific capacity than pure LFP upon high current density (2.55 A g^{-1}). Therefore, the electrode polarization extent of LMC@3_1 was far weaker than that of pure LFP. That meant high energy density under high power density was easier to achieve by adding MC for LFP-based devices. Moreover, the Tafel plot in Figure 5E was determined according to the various overpotentials and the logarithm of corresponding areal current densities (j, based on the product of the specific surface area of LFP and its mass in the cathode). Tafel regions at large overpotentials for both charge and discharge processes were then linearly fitted and the intercept at $\eta = 0$ represented the magnitude of the exchange current density (j_0), which was summarized in Figure 5F. The larger j_0 for LMC@3_1 compared with pure LFP implied the electrochemical reaction inside LFP particles was easier to occur with smaller electrochemical polarization in the presence of MC, consistent with the results in Figure 5B. Since the redox process did not occur in MC during charge/discharge, the above enhancement effect in LMC@3_1 cathode, i.e., the better Li-ion diffusion performance and the faster electrochemical reaction rate, could be ascribed to the establishment of local Li^+-rich region around MC due to its rapid EDLC effect, contributing to the fast Li intercalation/extraction kinetics.

According to the total mass of active materials in the cathode, the present LMC@3_1 cathode exhibited a maximum discharge energy density of 437 Wh kg^{-1} with a power density of 568 W kg^{-1} and maintained 104 Wh kg^{-1} with a maximum discharge power density of up to 23.4 kW kg^{-1}, proving the outstanding high-power characteristic of LFP/MC composite cathode owing to the enhanced Li intercalation kinetics of LFP with MC. Cycle performance of pure LFP and LMC@3_1 was also tested by 1C charge and 10C discharge and the electrochemical performance (specific capacity, energy density, power density, cycle life, *etc.*) of various reported LIBCs was summarized in Supplementary Table 4. Figure 6A showed the capacity of LMC@3_1 increased slightly in the previous dozens of cycles and nearly 100% capacity retention could be achieved after 1,000 cycles, far more excellent than that for pure LFP (31.5% retention). In addition, the

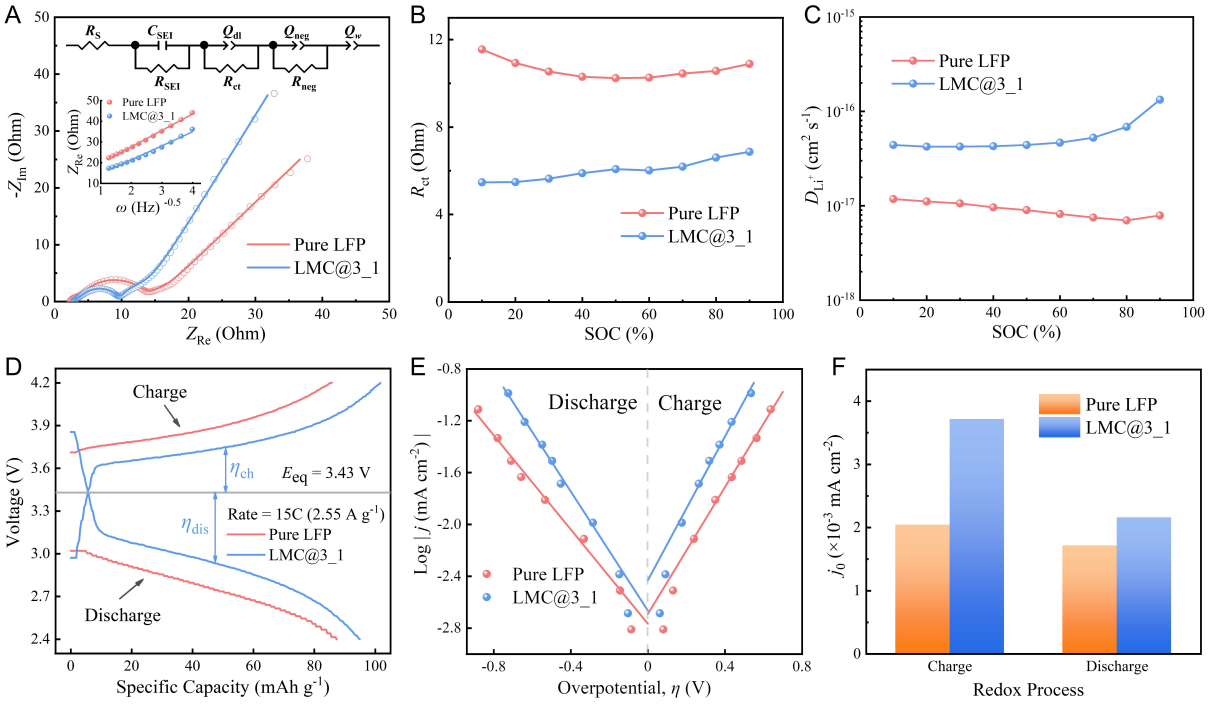

Figure 5. (A) EIS results at 50% SOC and the corresponding equivalent circuit model (inset: linear fitting of Z_{Re} to $\omega^{-0.5}$ in the frequency range of 0.01-0.1 Hz). (B) Charge transfer resistance (R_{ct}) at various SOC. (C) Solid-phase Li-ion diffusion coefficient (D_{Li^+}) at various SOC. (D) Voltage-capacity curves at 15C charge/discharge and the schematic illustration for calculating overpotential during charge (η_{ch}) and discharge (η_{dis}). (E) Tafel plot and the linear fitting in large overpotential regions. (F) Calculated exchange current density (j_0) during charge and discharge.

coulombic efficiency of LMC@3_1 was stable at about 100%, while it fluctuated greatly in the late cycles for pure LFP. In order to investigate the reasons for this cyclic difference, we disassembled the coin cells after cycling and characterized the electrode. An SEM image in Figure 6B revealed that severe fragmentation of LFP particles in pure LFP electrodes occurred after 1,000 cycles. The pristine single-crystal particles of around 100 nm [Supplementary Figure 1] were broken down into small fragments from a few to several tens of nanometers, with numerous cracks present. In contrast, although the fragmentation of LFP particles was also observed in the LMC@3_1 electrode [Figure 6C], the majority maintained their intact single-crystal morphology. We believed that the presence of MC favored better Li-ion diffusion performance, which facilitated more uniform Li-ion intercalation and extraction reactions and reduced volume changes of LFP particles during charge and discharge processes (as concluded in Figure 4D). Furthermore, the excellent conductivity of MC helped mitigate the impact of large currents on LFP particles as well[32]. Therefore, LFP particles in the LMC@3_1 electrode could maintain a more intact morphology after cycling, resulting in superior cycle performance. The *in-situ* XRD experiments of the cycled electrodes under 2C charge/discharge were also conducted to explore the phase transition process. Figure 6D showed that there were still noticeable intensity peaks at 29.4° and 35.3° at the end of charge, indicating some LFP particles in cycled pure LFP electrode had not completed the Li extraction process (7.8 wt% LFP residual according to the Rietveld refinement result). This might be due to the severe fragmentation of LFP particles and the damage to the crystal structure after prolonged cycling, resulting in the deactivation of some LFP particles and, thus, a sharp decrease in capacity of the pure LFP electrode after cycling. In contrast, Figure 6E showed no intensity peak at 29.4° and 35.3° at the end of charge and no appearance of the $FePO_4$ phase at the end of discharge. This indicated that even after 1,000 cycles, the LMC@3_1 electrode could still undergo complete charge and discharge processes, thereby maintaining nearly 100% of the initial capacity. These results

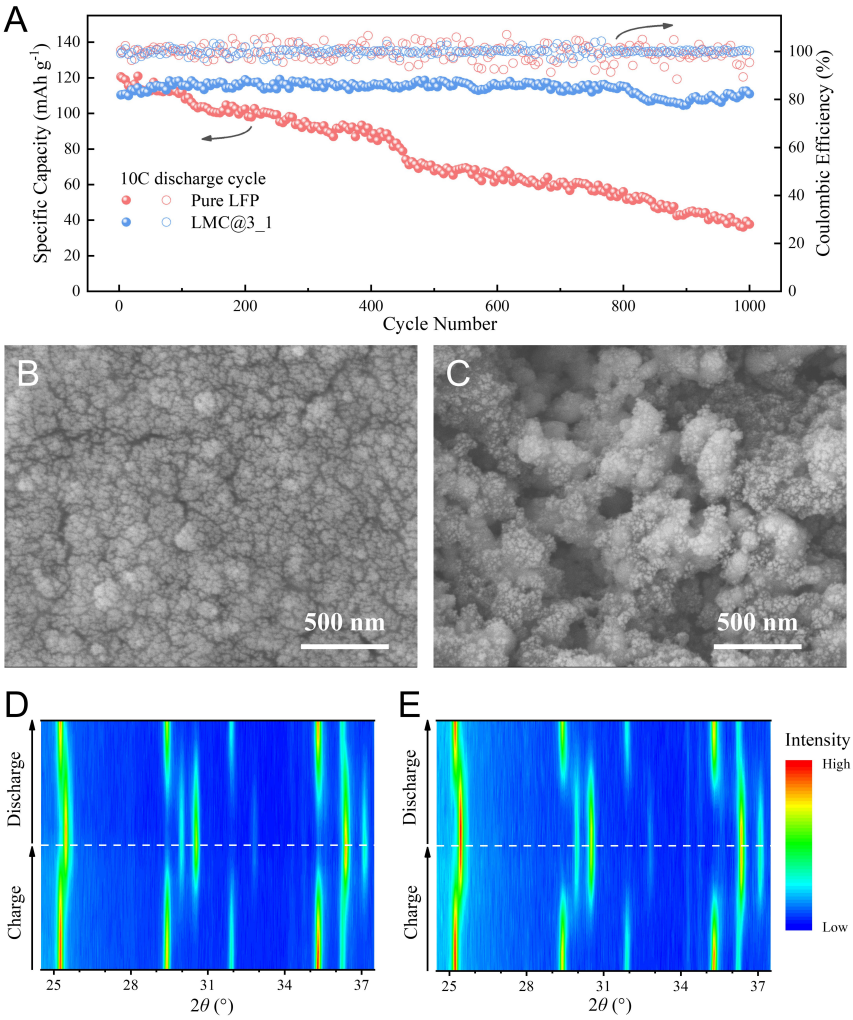

Figure 6. (A) Cyclic test of pure LFP and LMC@3_1 cathodes under 1C charge and 10C discharge. (B) SEM images of pure LFP electrode after cyclic test. (C) SEM images of LMC@3_1 electrode after cyclic test. Heat map of original *in-situ* XRD patterns under 2C charge/discharge for (D) pure LFP and (E) LMC@3_1 electrodes after cyclic test.

proved the rapid and sufficient Li-ion supply, the slight ion polarization and electron polarization for LMC@3_1 were favorable to a stable cycle life. Apparently, it was a very simple but robust method to increase the capacity, power density and cycle life of LFP-based devices by adding MC in large amounts.

CONCLUSIONS

This work proposed a concept that MC materials with high specific surface, high mesoporous volume and high conductivity could prompt the establishment of local Li^+-rich electrolyte region owing to the rapid EDLC effect, thus enhancing the Li intercalation kinetics of LFP nanoparticles in LMC composite cathode. A universal method for deriving the Li^+-rich concentration was provided as well. Using a single-particle model, we validated a favorable synergistic effect between LFP and MC to promote the capacity release of LFP, especially under a high discharge rate. The IDV value increased linearly with the MC content, proving that the Li-ion diffusion performance inside LFP particles was greatly improved in the presence of MC, which rendered a local Li^+-rich region for the Li intercalation process. Direct observation through HRTEM images revealed the extent of Li intercalation of LFP nanoparticles during high-rate discharge increased enormously with the addition of MC. Furthermore, quantitative analysis of the *in-situ* XRD results

confirmed the faster and more complete redox process occurred in LMC@3_1 compared with pure LFP, which was attributed to the enhancement effect of MC, including better electrical conductivity, higher Li-ion diffusion velocity and faster electrochemical reaction rate. As a result, LMC@3_1 could retain an energy density of 104 Wh kg^{-1} at a high power density of 23.4 kW kg^{-1} and maintain nearly 100% capacity retention after 1,000 cycles under 10C discharge, far more excellent than pure LFP, which demonstrated that LMC@3_1 was an outstanding cathode to fabricate the high-energy and high-power LIBCs with long cycle life. Future investigation would be focused on fabricating full cells toward the practical application calling for middle energy density (lower than Li-ion batteries but far higher than supercapacitors), high power density (far better than Li-ion batteries) and excellent cycle life (far better than Li-ion batteries).

DECLARATIONS

Acknowledgments

The authors acknowledge the financial support from the National Natural Science Foundation of China (No. 22109085).

Authors' contributions

Investigation, methodology, visualization, writing - original draft, writing - review & editing: Wei S
Investigation, writing - original draft, writing - review & editing: Cui C
Investigation, resources: Jin Y
Investigation: Wang J, Wang J, Li D
Conceptualization, writing - original draft, writing - review & editing: Qian W

Availability of data and materials

The data that support the findings of this study are available from the corresponding authors upon reasonable request.

Financial support and sponsorship

This work was financially supported by the National Natural Science Foundation of China (No. 22109085).

Conflicts of interest

All authors declared that there are no conflicts of interest.

Ethical approval and consent to participate

Not applicable.

Consent for publication

Not applicable.

Copyright

© The Author(s) 2024.

REFERENCES

1. Gür TM. Review of electrical energy storage technologies, materials and systems: challenges and prospects for large-scale grid storage. *Energy Environ Sci* 2018;11:2696-767. DOI
2. Bullich-massagué E, Cifuentes-garcía F, Glenny-crende I, et al. A review of energy storage technologies for large scale photovoltaic power plants. *Appl Energy* 2020;274:115213. DOI
3. Yan Y, Zeng T, Liu S, Shu C, Zeng Y. Lithium metal stabilization for next-generation lithium-based batteries: from fundamental chemistry to advanced characterization and effective protection. *Energy Mater* 2023;3:300002. DOI
4. Deng S, Wang H, Liu H, Liu J, Yan H. Research progress in improving the rate performance of $LiFePO_4$ cathode materials. *Nano-*

Micro Lett 2014;6:209-26. DOI
5. Heubner C, Nikolowski K, Reuber S, Schneider M, Wolter M, Michaelis A. Recent insights into rate performance limitations of Li-ion batteries. *Batteries Supercaps* 2021;4:268-85. DOI
6. Wu R, Xia G, Shen S, Zhu F, Jiang F, Zhang J. Soft-templated $LiFePO_4$/mesoporous carbon nanosheets (LFP/meso-CNSs) nanocomposite as the cathode material of lithium ion batteries. *RSC Adv* 2014;4:21325-31. DOI
7. Khan S, Raj RP, Mohan TV, Bhuvaneswari S, Varadaraju UV, Selvam P. Electrochemical performance of nano-$LiFePO_4$ embedded ordered mesoporous nitrogenous carbon composite as cathode material for Li-ion battery applications. *J Electroanal Chem* 2019;848:113242. DOI
8. Khan S, Raj RP, Rama Mohan TV, Selvam P. Electrochemical performance of nano-sized $LiFePO_4$-embedded 3D-cubic ordered mesoporous carbon and nitrogenous carbon composites. *RSC Adv* 2020;10:30406-14. DOI PubMed PMC
9. Kim DW, Hwang SM, Yoo JB, Kim Y. Electrode engineering with CNTs to enhance the electrochemical performance of $LiNi_{0.6}Co_{0.2}Mn_{0.2}O_2$ cathodes with commercial level design parameters. *ChemElectroChem* 2020;7:2621-8. DOI
10. Ghiyasiyan-arani M, Salavati-niasari M. Strategic design and electrochemical behaviors of Li-ion battery cathode nanocomposite materials based on AlV_3O_9 with carbon nanostructures. *Compos Part B Eng* 2020;183:107734. DOI
11. Yin L, Geng Z, Chien Y, et al. Implementing intermittent current interruption into Li-ion cell modelling for improved battery diagnostics. *Electrochim Acta* 2022;427:140888. DOI
12. Millares MFC, Takeuchi ES, Takeuchi KJ, Marschilok AC, Bock DC. Optimization of electrolyte volume in lithium-ion pouch-type cells. *MRS Adv* 2023;8:381-5. DOI
13. Wang L, Zhen M, Hu Z. Status and prospects of electrocatalysts for lithium-sulfur battery under lean electrolyte and high sulfur loading conditions. *Chem Eng J* 2023;452:139344. DOI
14. Xue S, Wang J, Xia Y, et al. Mesoporous carbon as conductive additive to improve the high-rate charge/discharge capacity of lithium-ion batteries. *Energy Technol* 2022;10:2200472. DOI
15. Stępień D, Zhao Z, Dsoke S. Shift to post-Li-ion capacitors: electrochemical behavior of activated carbon electrodes in Li-, Na- and K-salt containing organic electrolytes. *J Electrochem Soc* 2018;165:A2807-14. DOI
16. Zou K, Cai P, Deng X, et al. Revealing dual capacitive mechanism of carbon cathode toward ultrafast quasi-solid-state lithium ion capacitors. *J Energy Chem* 2021;60:209-21. DOI
17. Liu W, Zhang X, Xu Y, et al. Recent advances on carbon-based materials for high performance lithium-ion capacitors. *Batteries Supercaps* 2021;4:407-28. DOI
18. Sun X, Zhang X, Zhang H, Xu N, Wang K, Ma Y. High performance lithium-ion hybrid capacitors with pre-lithiated hard carbon anodes and bifunctional cathode electrodes. *J Power Sources* 2014;270:318-25. DOI
19. Yan J, Chen XJ, Shellikeri A, et al. Influence of Lithium iron phosphate positive electrode material to hybrid lithium-ion battery capacitor (H-LIBC) energy storage devices. *J Electrochem Soc* 2018;165:A2774-80. DOI
20. Hagen M, Yan J, Cao W, et al. Hybrid lithium-ion battery-capacitor energy storage device with hybrid composite cathode based on activated carbon/$LiNi_{0.5}Co_{0.2}Mn_{0.3}O_2$. *J Power Sources* 2019;433:126689. DOI
21. Lee SH, Huang C, Grant PS. High energy lithium ion capacitors using hybrid cathodes comprising electrical double layer and intercalation host multi-layers. *Energy Stor Mater* 2020;33:408-15. DOI
22. Guo Z, Liu Z, Sun X, et al. Probing current contribution of lithium-ion battery/lithium-ion capacitor multi-structure hybrid systems. *J Power Sources* 2022;548:232016. DOI
23. Han Y, Wang Z, Xie L, et al. Revealing the accelerated reaction kinetic of Ni-rich cathodes by activated carbons for high performance lithium-ion batteries. *Carbon* 2023;203:445-54. DOI
24. Yang Z, Tian J, Ye Z, et al. High energy and high power density supercapacitor with 3D Al foam-based thick graphene electrode: Fabrication and simulation. *Energy Stor Mater* 2020;33:18-25. DOI
25. Yang Z, Wang J, Cui C, et al. High power density & energy density Li-ion battery with aluminum foam enhanced electrode: fabrication and simulation. *J Power Sources* 2022;524:230977. DOI
26. Shellikeri A, Hung I, Gan Z, Zheng J. *In Situ* NMR tracks real-time Li ion movement in hybrid supercapacitor-battery device. *J Phys Chem C* 2016;120:6314-23. DOI
27. Shellikeri A, Yturriaga S, Zheng J, et al. Hybrid lithium-ion capacitor with $LiFePO_4$/AC composite cathode - Long term cycle life study, rate effect and charge sharing analysis. *J Power Sources* 2018;392:285-95. DOI
28. Jin L, Zheng J, Wu Q, et al. Exploiting a hybrid lithium ion power source with a high energy density over 30 Wh/kg. *Mater Today Energy* 2018;7:51-7. DOI
29. Guan Y, Shen J, Wei X, et al. $LiFePO_4$/activated carbon/graphene composite with capacitive-battery characteristics for superior high-rate lithium-ion storage. *Electrochim Acta* 2019;294:148-55. DOI
30. Hu X, Huai Y, Lin Z, Suo J, Deng Z. A ($LiFePO_4$-AC)/$Li_4Ti_5O_{12}$ hybrid battery capacitor. *J Electrochem Soc* 2007;154:A1026. DOI
31. Böckenfeld N, Placke T, Winter M, Passerini S, Balducci A. The influence of activated carbon on the performance of lithium iron phosphate based electrodes. *Electrochim Acta* 2012;76:130-6. DOI
32. Wang B, Wang Q, Xu B, Liu T, Wang D, Zhao G. The synergy effect on Li storage of $LiFePO_4$ with activated carbon modifications. *RSC Adv* 2013;3:20024. DOI
33. Padhi AK, Nanjundaswamy KS, Goodenough JB. Phospho-olivines as positive-electrode materials for rechargeable lithium batteries. *J Electrochem Soc* 1997;144:1188-94. DOI

34. Andersson A, Thomas J. The source of first-cycle capacity loss in $LiFePO_4$. *J Power Sources* 2001;97-8:498-502. DOI
35. Srinivasan V, Newman J. Discharge model for the lithium iron-phosphate electrode. *J Electrochem Soc* 2004;151:A1517-29. DOI
36. Yamada A, Koizumi H, Sonoyama N, Kanno R. Phase change in Li_xFePO_4. *Electrochem Solid State Lett* 2005;8:A409. DOI
37. Saikia D, Deka JR, Chou C, Lin C, Yang Y, Kao H. Encapsulation of $LiFePO_4$ nanoparticles into 3D interpenetrating ordered mesoporous carbon as a high-performance cathode for lithium-ion batteries exceeding theoretical capacity. *ACS Appl Energy Mater* 2019;2:1121-33. DOI
38. Cheng F, Li D, Lu A, Li W. Controllable synthesis of high loading $LiFePO_4$/C nanocomposites using bimodal mesoporous carbon as support for high power Li-ion battery cathodes. *J Energy Chem* 2013;22:907-13. DOI
39. Delmas C, Maccario M, Croguennec L, Le Cras F, Weill F. Lithium deintercalation in $LiFePO_4$ nanoparticles via a domino-cascade model. *Nat Mater* 2008;7:665-71. DOI
40. Orikasa Y, Maeda T, Koyama Y, et al. Direct observation of a metastable crystal phase of Li_xFePO_4 under electrochemical phase transition. *J Am Chem Soc* 2013;135:5497-500. DOI
41. Takahashi I, Mori T, Yoshinari T, et al. Irreversible phase transition between $LiFePO_4$ and $FePO_4$ during high-rate charge-discharge reaction by operando X-ray diffraction. *J Power Sources* 2016;309:122-6. DOI
42. Chen G, Song X, Richardson TJ. Electron microscopy study of the $LiFePO_4$ to $FePO_4$ phase transition. *Electrochem Solid State Lett* 2006;9:A295. DOI
43. Laffont L, Delacourt C, Gibot P, et al. Study of the $LiFePO_4$/$FePO_4$ two-phase system by high-resolution electron energy loss spectroscopy. *Chem Mater* 2006;18:5520-9. DOI
44. Fan J, Chen J, Chen Y, et al. Hierarchical structure $LiFePO_4$@C synthesized by oleylamine-mediated method for low temperature applications. *J Mater Chem A* 2014;2:4870-3. DOI
45. Gaberscek M. Towards optimized preparation of cathode materials: how can modeling and concepts be used in practice. *J Power Sources* 2009;189:22-7. DOI
46. Varzi A, Ramirez-castro C, Balducci A, Passerini S. Performance and kinetics of $LiFePO_4$-carbon bi-material electrodes for hybrid devices: a comparative study between activated carbon and multi-walled carbon nanotubes. *J Power Sources* 2015;273:1016-22. DOI